



Z-scheme carbon-bridged Bi₂O₃/TiO₂ nanotube arrays to boost photoelectrochemical detection performance

Yajun Pang^{a,b}, Yuwei Li^{a,c}, Guangqing Xu^{a,d,**}, Yating Hu^b, Zongkui Kou^{b,*}, Qiang Feng^a, Jun Lv^{a,d}, Yong Zhang^{a,d}, John Wang^b, Yucheng Wu^{a,d}

^a School of Materials Science and Engineering, and Key Laboratory of Advanced Functional Materials and Devices of Anhui Province, Hefei University of Technology, Hefei, 230009, China

^b Department of Materials Science and Engineering, National University of Singapore, Singapore, 117574, Singapore

^c School of Physics and Technology, Wuhan University, Wuhan, 430072, China

^d China International S&T Cooperation Base for Advanced Energy and Environmental Materials, Hefei, 230009, China

ARTICLE INFO

Keywords:

TiO₂ nanotube arrays
Carbon-bridged
Metal oxide nanocrystals
Z-scheme
Photoelectrochemical detection

ABSTRACT

An effective photoelectrochemical sensor is urgently needed for monitoring of the environmental pollution caused by organic wastes. In this work, we report a facile *in-situ* illumination-assisted process to introduce uniform metal oxide (Bi₂O₃) nanocrystals of 2–3 nm in sizes on carbon bridged TiO₂ nanotube arrays (TiO₂ NTAs) (Bi₂O₃/C@TiO₂ NTAs), in which the carbon functions as both electron trapping for high efficiency and system integration. The Bi₂O₃/C@TiO₂ NTAs thus made exhibit a highly selective photoelectrochemical determination performance, with low background photocurrent (derived from the decomposition of water) and high detection current (derived from the decomposition of organics target). In particular, the current detection of the Bi₂O₃/C@TiO₂ NTAs is 3.38 times higher than that of the pristine TiO₂ NTAs. To understand the key working principles involved, they are scrutinized by probing into the photoelectrochemical reaction process, including the light absorption, charge separation and transfer, and surface reactions. With the novel Z-scheme heterostructure system being achieved with Bi₂O₃/C@TiO₂ NTAs, the present work demonstrates the potential of metal oxides with uniform size in nanometer range and conductor-bridged strategy in creating Z-scheme heterostructure system with high photoelectrochemical detection performance for organics.

1. Introduction

With the rapid urbanization and industrialization, environmental issues caused by water pollution are becoming increasingly serious, as more and more pollutants are being produced and dumped into the water systems [1,2]. Effective monitoring of water quality is an essential step for environmental control and water treatments, where chemical oxygen demand (COD) is one of the widely used indicators in water quality analysis. It is also of high importance for sewage treatment operation, sewage monitoring and pollution taxation [3,4]. The commonly-used K₂Cr₂O₇ method experiences long-term reflux for a complete oxidation. It also employs noble, corrosive and toxic chemicals. Therefore, there is an urgent need for a rapid, environmental friendly and effective system for wastewater COD analysis [5].

TiO₂ nanotube arrays (TiO₂ NTAs) are known to be a favorable

candidate in photocatalytic degradation as well as detection of organic pollutants owing to their structural architectures and the unique properties of chemical inertness and stability, electrical conductivity, photostability, and high efficiency [6–11]. A photoelectrochemical sensor makes use of the relationship between photocatalytic oxidation and the COD, as has been detailed in one of our previous works [12], where high photoelectrochemical activities and appropriate surface reactions are required for COD determination. Unfortunately, the COD determination application of TiO₂ NTAs photoanode is largely limited by the poor conductivity, wide band gap (Anatase: 3.2 eV, Rutile: 3.0 eV), fast recombination rate, and improper indirect oxidation of organics by the hydroxyl radicals (·OH) during the photoelectrochemical process [7,13–19].

As a typical p-type semiconductor material, Bi₂O₃ has been in combination with TiO₂ in several applications. For example, the p-n

* Corresponding author.

** Corresponding author at: School of Materials Science and Engineering, and Key Laboratory of Advanced Functional Materials and Devices of Anhui Province, Hefei University of Technology, Hefei, 230009, China.

E-mail addresses: gqxu1979@hfut.edu.cn (G. Xu), msekz@nus.edu.sg (Z. Kou).

<https://doi.org/10.1016/j.apcatb.2019.01.077>

Received 10 November 2018; Received in revised form 23 January 2019; Accepted 27 January 2019

Available online 10 February 2019

0926-3373/ © 2019 Elsevier B.V. All rights reserved.

$\text{Bi}_2\text{O}_3\text{-TiO}_2$ heterojunction is considered to be an effective strategy for amending the surface reactions, due to the presence of an internal electric field at the interface. There have been several other reports on the $\text{Bi}_2\text{O}_3\text{-TiO}_2$ composites synthesized by hydrothermal, electrochemical, and electrodeposition methods [20–24]. In general, these techniques have poor control over size and morphology, although some of them have shown interesting behavior. Due to the accumulation of photo-generated electrons and holes in the band with lower redox potential, the separation of charge carriers increases while the redox ability is inhibited. As a result, the heterojunction photocatalysts cannot achieve a strong redox ability and high electron hole separation simultaneously. Therefore, considerable attention has been paid to the Z-scheme structure with electron mediator, which not only enhances the separation efficiency of photo-generated charge pairs, but also preserves excellent redox ability. Both metals and non-metals (e.g. Au, Ag, graphene or rGO) have been investigated, where an electron mediator is required in the construction of Z-scheme heterostructures [25–33]. Herein, as a proof of concept, we present a facile *in-situ* illumination-assisted process for obtaining uniform Bi_2O_3 nanocrystals of 2–3 nm in sizes on TiO_2 NTAs. In the *in-situ* process, carbon is introduced as electron trapping for both high efficiency and system integration. Interestingly, in the Z-scheme based on this new system, the “bridging” carbon between Bi_2O_3 and TiO_2 help produce a higher charge separation efficiency and preserve a stronger redox ability. When applied to photoelectrochemical detection, the as-obtained $\text{Bi}_2\text{O}_3\text{/C@TiO}_2$ NTAs presents a highly selective photoelectrochemical determination performance with negligible background photocurrent and strong detection current, compared favorably with TiO_2 , C@TiO_2 , and $\text{Bi}_2\text{O}_3\text{/TiO}_2$. To properly understand the mechanism behind, we have studied the photoelectrochemical detection sensor by looking into the entire photoelectrochemical process.

2. Experimental section

2.1. Materials

Bismuth nitrate pentahydrate ($\text{Bi}(\text{NO}_3)_3 \cdot 5\text{H}_2\text{O}$), pluronic F-127, methanol (CH_3OH), glucose, and ammonium fluoride (NH_4F) were purchased from Aladdin Industrial Corporation. Disodium hydrogen phosphate (Na_2HPO_4), sodium dihydrogen phosphate (NaH_2PO_4), ammonium oxalate (AO), isopropanol (IPA), and ethylene glycol were purchased from Sinopharm Chemical Reagent Co., Ltd. All reagents were of analytical grade and used as received without further purification. Deionized water was used in the synthesis process.

2.2. Synthesis of TiO_2 NTAs and C@TiO_2 NTAs

TiO_2 NTAs were synthesized by an electrochemical anodization process which has been described in a previous work [34]. The anodized TiO_2 NTAs were calcined at 500°C for 2 h in air and N_2 atmosphere for developing anatase TiO_2 NTAs and C@TiO_2 NTAs, respectively, as shown in Scheme 1.

2.3. Synthesis of $\text{Bi}_2\text{O}_3\text{/TiO}_2$ and $\text{Bi}_2\text{O}_3\text{/C@TiO}_2$ NTAs

Firstly, TiO_2 or C@TiO_2 NTAs were immersed in a mixed aqueous solution containing 10 mM $\text{Bi}(\text{NO}_3)_3$ and pluronic F127 solutes for 5 min, where F127 is an important dispersant for obtaining a uniformly dispersed Bi source. The sample was then transferred into 1 M methanol with ultraviolet light illumination for 2 min *in-situ* reaction. Finally, Bi_2O_3 nanocrystals of 2–3 nm sizes were modified on TiO_2 or C@TiO_2 NTAs (Scheme. 1).

2.4. Characterization

Phase analysis of X-ray diffraction was conducted using X-ray

diffraction (X'Pert PRO MPD, Netherland). Raman spectra were acquired using a LabRam HR Evolution (Horiba Jobin Yvon, France) instrument, which was performed with an excitation wavelength of 532 nm. Morphologies of the samples were characterized using scanning electron microscope (SEM, Hitachi SU8020) and transmission electron microscope (TEM, Jeol JEM-2100 F). Atomic force microscopy (AFM) was performed on a commercial conductive AFM module (ORCA, Asylum Research, USA) with conductive Pt-coated Si tips. The chemical states of the samples were studied using X-ray photoelectron spectroscopy (XPS, Thermo ESCALAB250Xi), and the binding energy of C 1s peak at 284.6 eV was taken as an internal standard. UV–vis optical absorptions were recorded with a Hitachi UV-3600 spectrophotometer using BaSO_4 as the reference. Photoluminescence (PL) studies were conducted using a F-4500 FL Spectrophotometer (Shimadzu, Japan) with an excitation wavelength of 315 nm and a collection wavelength range of 350–600 nm, to investigate the charge carries and monitor the concentration of $\cdot\text{OH}$ radicals, respectively. Room-temperature ESR spectra of $\cdot\text{O}_2^-$ trapped by DMPO were obtained using a JEOL JES FA200 ESR spectrometer (300 K, 9.063 GHz, X-band). The microwave power employed, modulation frequency and amplitude were 1 mW, 100 kHz and 0.35 mT, respectively.

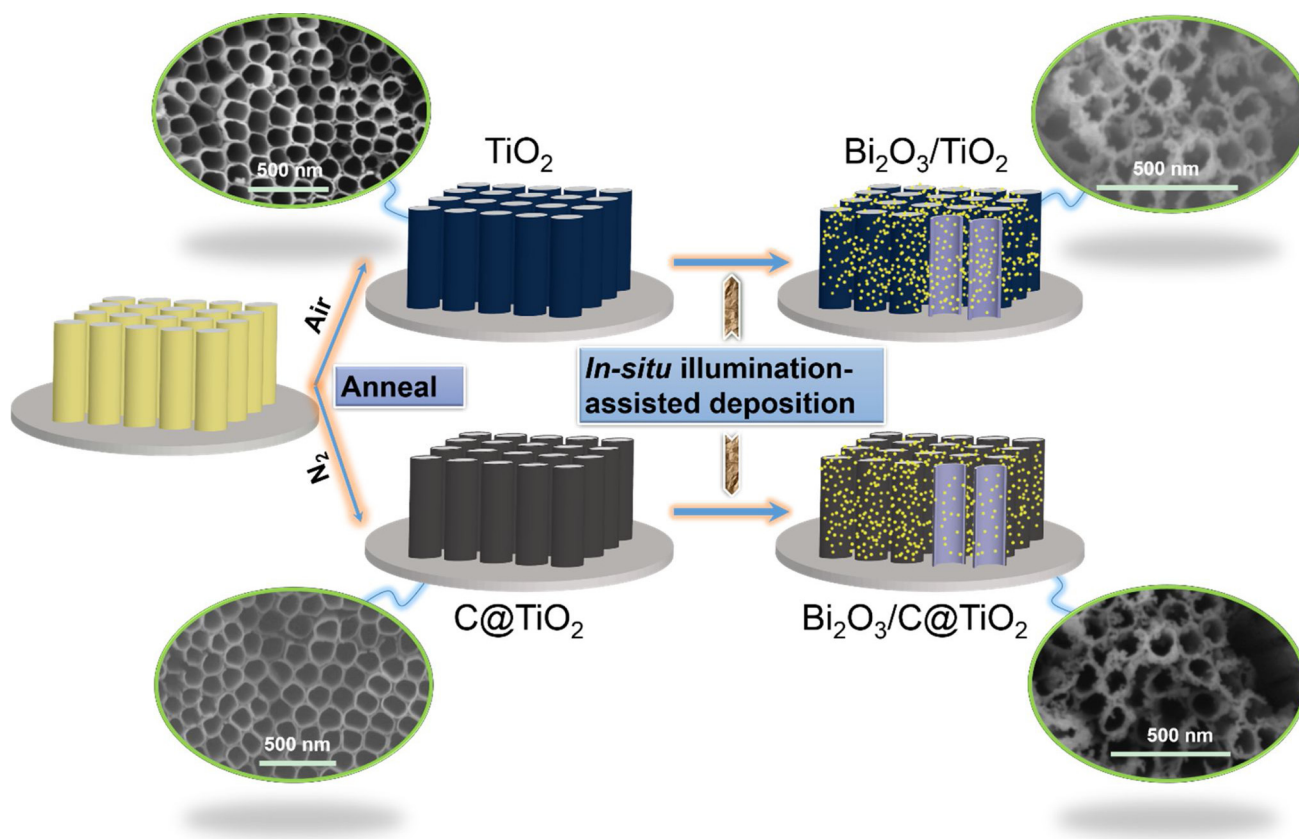
2.5. Photoelectrochemical test

Photoelectrochemical measurements were conducted using a home-made flow-injection photoelectrochemical cell, as illustrated in Scheme S1. The photoelectrochemical system is a thin reactor combined with an ultraviolet (UV) LED source with a fixed wavelength of 365 nm, a spot diameter of 10 mm and adjustable optical power ranging from 0 to 1200 mW/cm^2 . The standard three-electrode cell was composed of the sample as the working electrode, an Ag/AgCl reference electrode and a Pt wire auxiliary electrode, respectively. The supporting electrolyte used in electrochemical measurement was 0.05 M phosphate buffer solution ($\text{pH} = 7$) (PBS), obtained by adjusting the ratio of Na_2HPO_4 to NaH_2PO_4 . Glucose was used as the target organics for photoelectrochemical determination measurements. The measurements were conducted as follows. Firstly, the PBS was pumped into the cell. Once a steady-state current was reached, a fixed concentration of target organics solution was injected into the thin cell to obtain an increment of photocurrent, and this step is repeated many times to obtain a proper relationship between the current increment and glucose concentration. On this basis, the properties determined for photoelectrochemical COD detection included COD detection range, sensitivity and detection limit. The EIS curves were recorded in the frequency range from 10^{-1} to 10^5 at a potential of 0.1 V and an amplitude of 0.005 V. All experiments were conducted in ambient conditions.

3. Results and discussion

3.1. Structural characterization

The as-synthesized TiO_2 , C@TiO_2 and $\text{Bi}_2\text{O}_3\text{/C@TiO}_2$ NTAs were analyzed using XRD and Raman spectrometers as shown in Fig. 1a–b. Upon annealing at 500°C both in air and N_2 atmosphere, all diffraction peaks can be assigned to anatase TiO_2 and metallic Ti substrate, as shown in the XRD patterns of TiO_2 and C@TiO_2 NTAs in Fig. 1a. No additional peaks from carbon can be found in the pattern of C@TiO_2 NTAs, due to the low crystallinity or small thickness of the carbon layer on TiO_2 NTAs [35,36]. New peaks appear at 2θ of 21.18° and 44.98° in $\text{Bi}_2\text{O}_3\text{/C@TiO}_2$ NTAs, which can be ascribed to the (211) and (431) planes of Bi_2O_3 , as shown in the XRD pattern of $\text{Bi}_2\text{O}_3\text{/C@TiO}_2$ NTAs [37,38], indicating that Bi_2O_3 nanocrystals have been successfully deposited on TiO_2 or C@TiO_2 NTAs by the illumination-assisted deposition process. Raman spectra of the as-prepared samples were also measured for further studies, as shown in Fig. 1b. The Raman peaks at approximately 148, 398, 520, 642 cm^{-1} can be designated as the E_g ,



Scheme 1. Schematic diagram showing the procedures for sample preparations.

B_{1g} , B_{1g} or A_{1g} , E_g modes of the anatase phase TiO_2 , respectively [39,40]. The characteristic D and G bands are found in $C@TiO_2$ and $Bi_2O_3/C@TiO_2$ NTAs, in the high resolution spectra, which can be assigned to carbon [41]. Those structural characteristics demonstrate that both carbon and Bi_2O_3 are assembled on TiO_2 NTAs [42].

Top and cross-sectional SEM morphologies of $Bi_2O_3/C@TiO_2$ NTAs are shown in Fig. 1c. In comparison among TiO_2 , $C@TiO_2$, Bi_2O_3/TiO_2 NTAs, a highly-ordered and uniform tubular structure can be observed

in Fig. 1c and Fig. S1a-c. Almost no difference in morphologies is observed when comparing between TiO_2 and $C@TiO_2$ NTAs. The formation of the carbon layer on the outer surface of nanotubes had been observed in the TEM study. With the *in-situ* illumination-assisted process, Bi_2O_3 nanocrystals with small sizes were deposited on the tube mouths and walls of either TiO_2 NTAs or $C@TiO_2$ NTAs. Obviously, this *in-situ* illumination-assisted process had effectively suppressed the aggregation of Bi_2O_3 nanocrystals on the nanotubes, without destroying

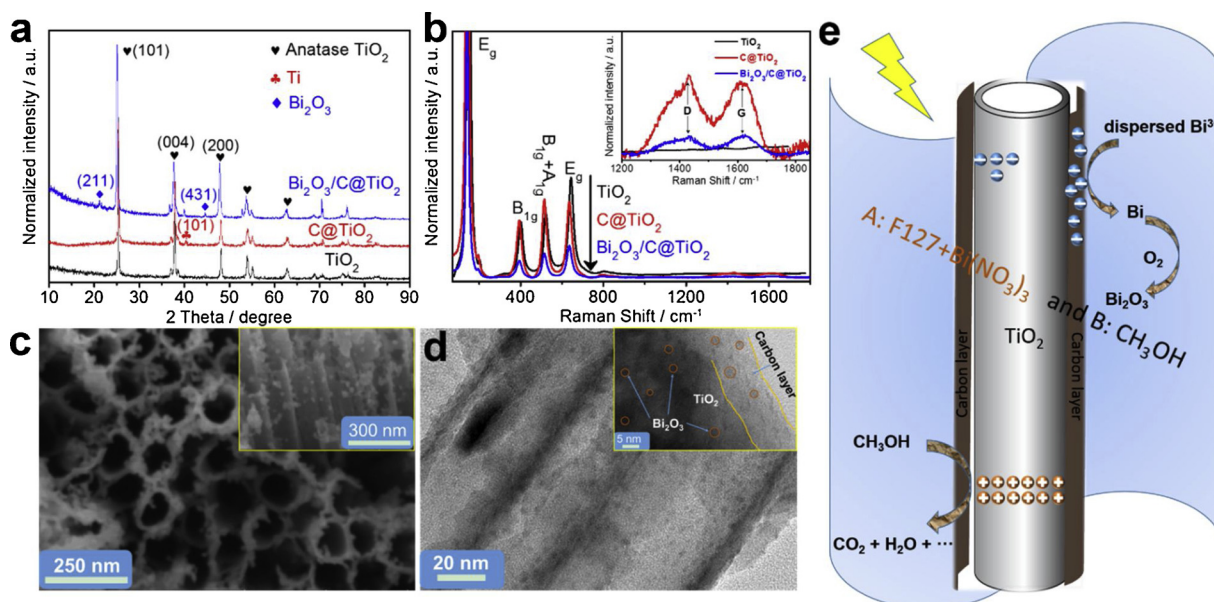
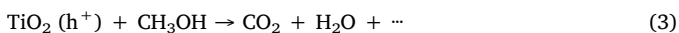


Fig. 1. X-ray diffraction patterns (a), Raman spectra (b) of TiO_2 NTAs, $C@TiO_2$ NTAs and $Bi_2O_3/C@TiO_2$ NTAs; Scanning electron micrographs (c), Transmission electron micrographs (d), and formation mechanism (e) of $Bi_2O_3/C@TiO_2$ NTAs.

the ordered tubular structure of TiO₂ NTAs or C@TiO₂ NTAs [43].

Morphologies of TiO₂, C@TiO₂, Bi₂O₃/TiO₂ and Bi₂O₃/C@TiO₂ NTAs studied using TEM are shown in Fig. 1d and Fig. S1d-f. A comparison between TiO₂ and C@TiO₂ NTAs confirms the carbon layer of several nanometers on the nanotube of TiO₂ (Fig. S1d-e). The carbon layer appears in an amorphous structure, as shown by the high resolution pattern in the up-right inset, which is consistent with the result of Raman spectra shown in Fig. 1b. Bi₂O₃ nanocrystals of refined sizes were observed on TiO₂ tube walls, as shown in Fig. 1d and Fig. S1. They were well-distributed in and out of the nanotubes of Bi₂O₃/TiO₂ and Bi₂O₃/C@TiO₂ NTAs. The nanotube and nanocrystals size distributions of different samples are shown in Fig. S2, where the Bi₂O₃ nanocrystals are seen to distribute over the wall of nanotubes with the introduction of the carbon layer. Moreover, the EDS mapping image (Fig. S3) suggests that the Bi₂O₃ was uniformly attached on the TiO₂ nanotubes. There is a different surface configuration by the introduction of Bi₂O₃ nanoparticles, which is confirmed by the results of the top view AFM images (Fig. S4). In Bi₂O₃/C@TiO₂ NTAs, these nanocrystals were seen at the junction of carbon layer and TiO₂ nanotubes, which can be explained by the formation of Bi₂O₃ nanocrystals on TiO₂ or C@TiO₂ NTAs. The proposed reactions during the *in-situ* illumination-assisted modification of Bi₂O₃ nanocrystals are as follows, as shown in Fig. 1e. Pluronic F127 plays an import role as a dispersing agent in the Bi(NO₃)₃ solution, such that the active nano-Bi is formed by the reaction between the photo-generated electrons of TiO₂ with the dispersed Bi³⁺ under illumination. At the same time, the photo-generated holes of TiO₂ are captured by methanol (as holes trapping) to restrict the recombination of photo-generated electrons and holes. Hence, the Bi₂O₃ nanocrystals are formed between Bi and the dissolved O₂ in solution. The proposed reactions can be listed as follows:



As has been known, the free electrons prefer to transfer to the wall of TiO₂ nanotubes due to the introduction of the carbon layer (as an electrons trapping) on nanotubes, and the reaction between Bi³⁺ ions and electrons takes place at the junction.

The chemical components of samples were analyzed using XPS. The Bi 4f spectra can be deconvoluted into two peaks at 164.7 eV (Bi 4f_{5/2}) and 159.4 eV (Bi 4f_{7/2}), as shown in Fig. 2a. The binding energy between Bi 4f_{7/2} and Bi 4f_{5/2} is about 5.3 eV, showing the +3 valence of Bi element, indicating the presence of Bi₂O₃. Compared with Bi₂O₃ (158.6 eV and 163.9 eV), the positive shift of Bi₂O₃/C@TiO₂ sample indicates a strong interaction between Bi₂O₃ and TiO₂, and some electrons are transferred from Bi atom to the TiO₂ support [44]. The fitting of the Ti 2p signal (Fig. 2b) shows the +4 state for Ti on the surface of the as-prepared Bi₂O₃/C@TiO₂ NTAs. The C 1s fine XPS spectra of TiO₂ and Bi₂O₃/C@TiO₂ NTAs are shown in Fig. 2c and Fig. S5b, respectively. The contribution of 284.6 eV is mainly due to C_{in}, which is derived from the standard internal carbon during XPS measurements, while the contributions of 286.3 and 288.9 eV are attributed to C–OH (and C–O–C) and C=O (and COO), respectively. The C 1s signal of TiO₂ NTAs is derived from carbon pollutants adsorbed in the atmosphere, possibly hydrocarbons and carbonates. The significant increase in the C 1s signal of Bi₂O₃/C@TiO₂ NTAs is due to the formation of the carbon layer on the outer surface of TiO₂ NTAs [45,46]. These results are also consistent with the high C content of Bi₂O₃/C@TiO₂ NTAs sample. Furthermore, no C 1s peak at 281 eV is observed, which is due to the Ti–C bond, indicating that the carbon is not doped into the TiO₂ lattice [47]. The intimate contact between the

carbon layer and TiO₂ NTAs facilitates the charge separation and transfer, and the carbon layer can also enhance the photoelectrochemical properties of TiO₂ NTAs. The carbon layer not only helps to harvest more light, but also maintains a high reactivity of photo-generated electrons and holes by absorbing photo-generated electrons. In contrast to the lattice substitution in carbon-doped oxides, the carbon in the Bi₂O₃/C@TiO₂ NTA acts as a surface sensitizer to absorb light and acts as a medium to facilitate the charge separation and transfer. The high resolution spectra of O 1s are displayed in Fig. S5c. The oxygen on the surface of the sample exists at the binding energies of 530.3, 531.2 and 532.3 eV, wherein the main peak centered at 530.3 eV, and 531.2 eV can be attributed to the Ti–O and Bi–O bonds, respectively. The peak at 532.3 eV is attributed to the oxygen molecules adsorbed on the surface of the sample.

Fig. 2d shows the optical absorption spectra of TiO₂, C@TiO₂, Bi₂O₃/TiO₂ and Bi₂O₃/C@TiO₂ NTAs. In comparison with TiO₂ NTAs, C@TiO₂ NTAs shows much better absorption, which is also confirmed by the inset optical picture. As mentioned above, the carbon layer helps absorb light and reduce the light reflection [48,49]. The absorption of C@TiO₂ NTAs is enhanced at the wavelength of 365 nm, which is used as the light source in this work. The high optical absorption would be beneficial to the photoelectrochemical properties of TiO₂ NTAs. The optical absorption of TiO₂ or C@TiO₂ NTAs almost possesses no change after the modification of Bi₂O₃ nanocrystals, confirming that the optical activities are not the main factor in enhancing the photoelectrochemical performance.

3.2. Photoelectrochemical detection performances

During the PEC determination process, the photocatalyst decomposes water and organics simultaneously. However, this non-selective decomposition results in a relatively high background photocurrent signal (derived from the decomposition of water) which can greatly reduce the efficiency and sensitivity of the PEC detection sensor for organics in the wastewater. Here, in order to investigate the ability of the as-prepared materials to selectively decompose water and organics, Fig. 3a shows the background photocurrents and current responses to organics (derived from the decomposition of 0.1 mM glucose, as the target of organics) of TiO₂, C@TiO₂, Bi₂O₃/TiO₂ and Bi₂O₃/C@TiO₂ NTAs, which were tested by the amperometric method at an applied potential of 0.2 V in phosphate buffer solution (PBS). Compared with TiO₂ NTAs (172.40 μA·cm^{−2} and 10.19 μA·cm^{−2}), C@TiO₂ NTAs possess a higher photocurrent (191.50 μA·cm^{−2}) and a little enhanced current response to organics (16.79 μA·cm^{−2}). By modifying the Bi₂O₃ nanocrystals on TiO₂ or C@TiO₂ NTAs, a lower background photocurrent and a higher current response are obtained (Fig. 3b). The background photocurrent and current response of Bi₂O₃/TiO₂ NTAs are 55.65 μA·cm^{−2} and 24.50 μA·cm^{−2}, respectively. Bi₂O₃/C@TiO₂ NTAs show a little higher background photocurrent of 105.04 μA·cm^{−2}, while with an enhanced current response of 34.51 μA·cm^{−2}. It can be seen that, considering the background photocurrent and current response factors, Bi₂O₃/C@TiO₂ NTA exhibit the best potential in the selective photoelectrochemical detection applications. Additionally, it also shows a good stability towards a long-term current response (Fig. S6).

Fig. 3c shows the amperometric current responses of the four samples, i.e., TiO₂, C@TiO₂, Bi₂O₃/TiO₂ and Bi₂O₃/C@TiO₂ NTAs, with the successive addition of glucose (herein, the sequence of glucose injection is 10 μM twice, 20 μM twice, 40 μM once, 50 μM twice, and then 100 μM repeated.). All samples show excellent and rapid current response to COD increment. The current response vs. COD data (corresponding to the concentration of organics) is shown in Fig. 3d. The detection sensitivity and limit can be given from the linear part of the fitted curve. The detection limit (*dI*) performance can be calculated through the detection in sensitivity and current noise of photoelectrochemical COD sensors [50]. The current noise is obtained by the high resolution curve of current vs. time, as shown in Fig. S7, and determination performance

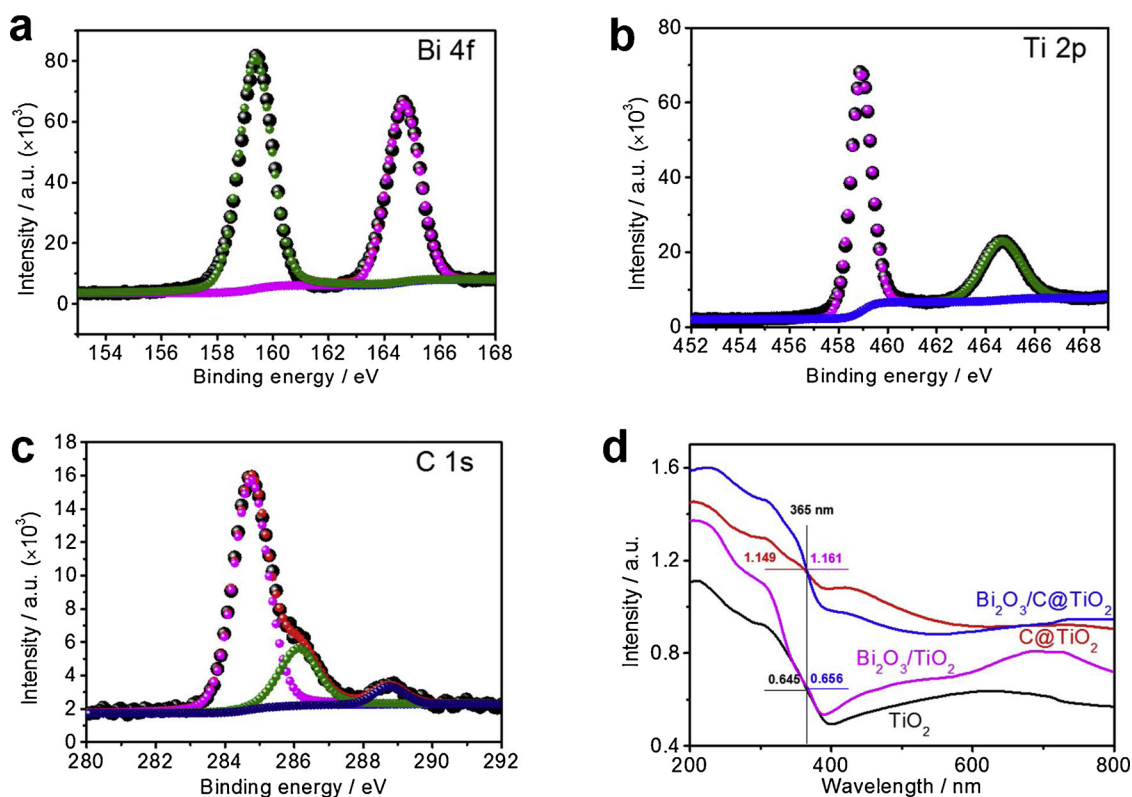


Fig. 2. High resolution spectra of Bi 4f (a), Ti 2p (b), and C 1s (c) of $\text{Bi}_2\text{O}_3/\text{C@TiO}_2$ NTAs; and Optical absorption spectra of TiO_2 , C@TiO_2 , $\text{Bi}_2\text{O}_3/\text{TiO}_2$ and $\text{Bi}_2\text{O}_3/\text{C@TiO}_2$ NTAs.

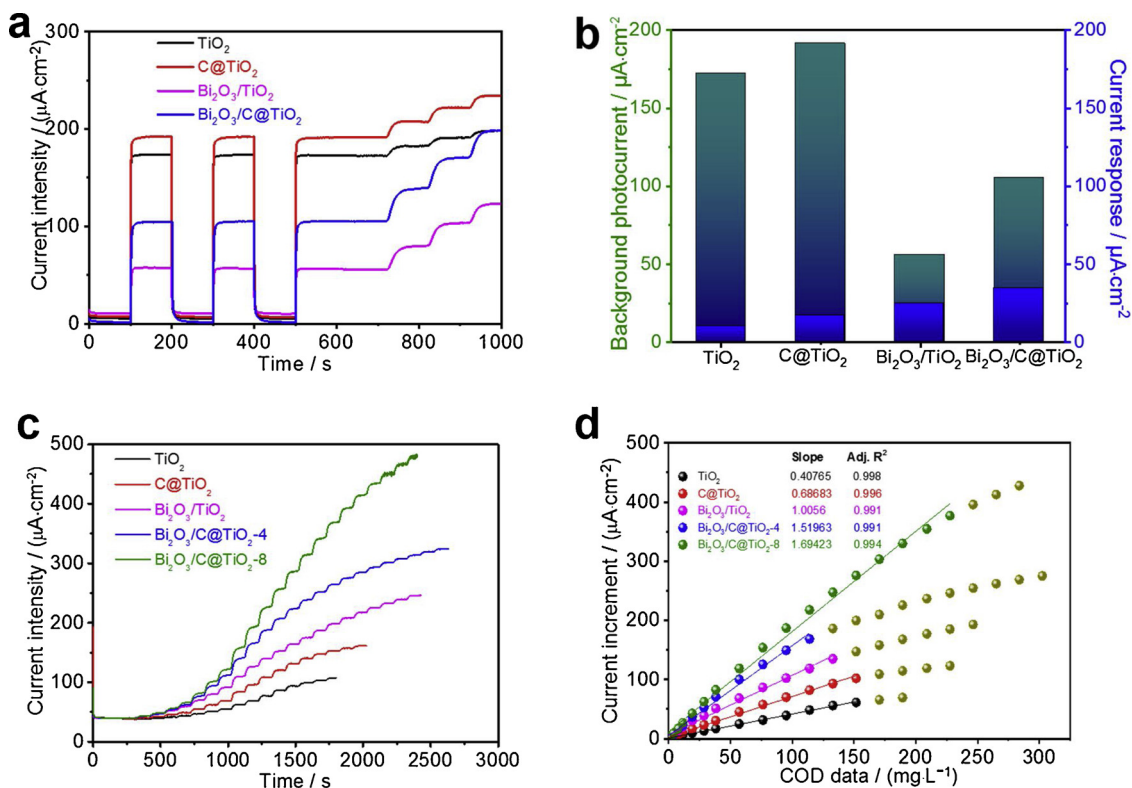


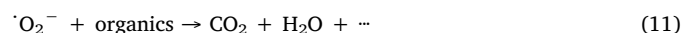
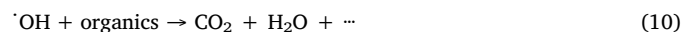
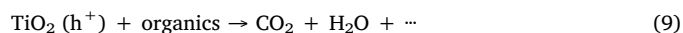
Fig. 3. Background photocurrents and current responses to 0.1 mM glucose (a, b); and amperometric current responses to successive additions of glucose: current–time curve (c), plot of current increment vs. COD data (d) of TiO_2 , C@TiO_2 , $\text{Bi}_2\text{O}_3/\text{TiO}_2$ and $\text{Bi}_2\text{O}_3/\text{C@TiO}_2$ NTAs.

parameters are listed in Table S2 for better comparison. C@TiO₂ NTAs (0.68683 $\mu\text{A}\cdot\text{cm}^{-2}/(\text{mg}\cdot\text{L}^{-1})$ of sensitivity and 1.957 $\text{mg}\cdot\text{L}^{-1}$ of detection limit) shows better detection performance than that of pristine TiO₂ NTAs (0.40765 $\mu\text{A}\cdot\text{cm}^{-2}/(\text{mg}\cdot\text{L}^{-1})$ and 3.341 $\text{mg}\cdot\text{L}^{-1}$). Furthermore, both Bi₂O₃/TiO₂ (1.0056 $\mu\text{A}\cdot\text{cm}^{-2}/(\text{mg}\cdot\text{L}^{-1})$ and 0.379 $\text{mg}\cdot\text{L}^{-1}$) and Bi₂O₃/C@TiO₂ NTAs (1.51963 $\mu\text{A}\cdot\text{cm}^{-2}/(\text{mg}\cdot\text{L}^{-1})$ and 0.296 $\text{mg}\cdot\text{L}^{-1}$) exhibit much better detection performance by the successful deposition of Bi₂O₃ nanocrystals. In addition, the current noise is also decreased at the same time, as shown in Table S2. One can include that the carbon-bridged Bi₂O₃/C@TiO₂ holds the best detection performance, including sensitivity and detection limit. The detection COD range could not be enhanced firmly. Hence, an optical output power with 8%, which is twice as high as the power previously tested, was applied to investigate the influence of optical power on the photoelectrochemical detection properties of Bi₂O₃/C@TiO₂ NTAs (defined as Bi₂O₃/C@TiO₂-8). The performance of detection COD range can be regulated by the increase of optical power.

3.3. Mechanism discussion

Based on the above characterization results, one can see that the optical absorption of C@TiO₂ NTAs is higher than that of pristine TiO₂ NTAs, which can enhance the photocurrent. However, as shown in Fig. 3a, the photocurrent of C@TiO₂ NTAs is by about 11% higher than that of TiO₂ NTAs, while the optical absorption is improved by 78% by the introduction of the carbon layer. Besides, the light absorption of Bi₂O₃/TiO₂ and Bi₂O₃/C@TiO₂ NTAs was not improved with the modification of nanocrystals. Therefore, the light absorption was not the key factor in boosting photoelectrochemical detection performance. The Bi₂O₃ nanocrystals also possesses a significant effect on the detection performance of TiO₂ or C@TiO₂.

According to above discussions, the photoelectrochemical reactions of TiO₂ during the detection process can be described as follows:



To get further insight into the detection process, electrochemical impedance spectroscopy (EIS) was used to study the charge transfer in the samples, as shown in Fig. 4a. The diameter of semicircle in the Nyquist diagram reflects the charge transfer process, in which a smaller diameter of the semicircle reveals a lower charge transfer resistance [51]. As shown in Fig. 4a, the diameter of C@TiO₂ NTAs is smaller than that of TiO₂ NTAs under UV light irradiation, indicating that the carbon layer on TiO₂ NTAs had considerably reduced the resistance of charge transfer, signifying its enhanced photoelectrochemical property [52]. However, a little higher charge transfer resistance of Bi₂O₃/TiO₂ and Bi₂O₃/C@TiO₂ NTAs was determined with the introduction of Bi₂O₃ nanocrystals, demonstrating that the Bi₂O₃ nanocrystals cannot improve the charge transfer ability in the system of either Bi₂O₃/TiO₂ or Bi₂O₃/C@TiO₂ NTAs. Bi₂O₃/C@TiO₂ NTAs possess a higher charge transferability than that of Bi₂O₃/TiO₂ NTAs, demonstrating that the carbon layer had acted as an excellent electron trapping for better electron-hole pairs transferring. The electron lifetime in photoanode can be correlated with the frequency peaks in Bode phase plots (Fig. S8). There is almost no change after the introduction of Bi₂O₃, demonstrating that the Bi₂O₃ nanocrystals cannot prolong the lifetime in either Bi₂O₃/TiO₂ or Bi₂O₃/C@TiO₂ NTAs. However, the Bi₂O₃/C@TiO₂ NTAs possess a longer electron lifetime when compared with the Bi₂O₃/TiO₂ NTAs, identifying that the carbon layer can prolong the

electron lifetime and facilitate charge transport.

To investigate the predominant active species and identify the major contributor to the organics determination in the photoelectrochemical reaction, and understand the reaction mechanism in depth, two typical scavengers, ammonium oxalate (AO) and isopropyl alcohol (IPA) were used in the study of the hole (h^+) and hydroxyl radical ($\cdot\text{OH}$), respectively [53,54], as shown in Fig. 4b and Fig. S9. Both AO and IPA additions enhance the photocurrent of TiO₂ NTAs from 167.6 $\mu\text{A}\cdot\text{cm}^{-2}$ to 227.0 $\mu\text{A}\cdot\text{cm}^{-2}$ and 307.3 $\mu\text{A}\cdot\text{cm}^{-2}$ respectively. The higher increment of IPA addition than that of AO addition indicates that $\cdot\text{OH}$ radical is more crucial than h^+ in the photoelectrochemical reaction. C@TiO₂ NTAs show a similar increase of photocurrent with that of TiO₂ NTAs, when adding trapping agents, indicating that the carbon layer does not change the surface reaction of the anode during the photoelectrochemical process. However, a dramatic change appears when AO is added in the Bi₂O₃/TiO₂ system. The photocurrent increases from 71.0 $\mu\text{A}\cdot\text{cm}^{-2}$ to 373.7 $\mu\text{A}\cdot\text{cm}^{-2}$, showing an increment of almost 5 times. Moreover, holes appear to play an even bigger role in photocurrent of Bi₂O₃/TiO₂ NTAs than that of $\cdot\text{OH}$ radicals. It is interesting to note that, when carbon layer is introduced between Bi₂O₃ and TiO₂, Bi₂O₃/C@TiO₂ NTAs show a similar surface reaction to that of TiO₂ and C@TiO₂ NTAs with a bigger effect of $\cdot\text{OH}$ radicals than that of holes in the photoelectrochemical process. This suggests a different surface reaction mechanism between Bi₂O₃/TiO₂ and Bi₂O₃/C@TiO₂ in boosting the photoelectrochemical detection.

The concentration of $\cdot\text{OH}$ plays a key role in the photoelectrochemical detection process of organics by TiO₂ and TiO₂ NTAs. The analysis of $\cdot\text{OH}$ radicals were analyzed by measuring the fluorescence intensity of the 2-hydroxyterephthalic acid (HOTP) at 420 nm, when excited by light at 315 nm, which is the product of terephthalic acid (TA) after the reaction with $\cdot\text{OH}$ radicals (Fig. 4c-d) [55,56]. It can be seen that the emission intensity of C@TiO₂ NTAs is a bit higher than that of TiO₂ NTAs, which means a higher $\cdot\text{OH}$ concentration in the photoelectrochemical process, due to the enhanced optical absorption and low recombination rate of electron-hole pairs. A low emission intensity is obtained with the modification of Bi₂O₃, confirming a lower productivity of $\cdot\text{OH}$ radical in the system of either Bi₂O₃/TiO₂ or Bi₂O₃/C@TiO₂.

TiO₂ NTAs possess different photoelectrochemical detection mechanisms, by the introduction of the carbon layer and Bi₂O₃ nanocrystals. Fig. 5 presents a proposed determination mechanism for the TiO₂, C@TiO₂, Bi₂O₃/TiO₂ and Bi₂O₃/C@TiO₂ NTAs, respectively. Firstly, the photogenerated electrons and holes are produced under UV light illumination, the recombination of electron-hole pairs cannot be refrained during the charge transfer process, as illustrated in process (2) (Fig. 5a). The $\cdot\text{OH}$ and $\cdot\text{O}_2^-$ radicals, with the oxidation ability will be produced by the reaction containing holes and electrons respectively (process (3) and (4)) (Fig. 5a) [57]. For C@TiO₂, as an electron trapping, the carbon layer promotes the electrons transfer from the conduction band (CB) of TiO₂ to carbon layer [44]. Both TiO₂ and Bi₂O₃ in Bi₂O₃/TiO₂ NTAs are excited simultaneously under the UV light illumination. The difference of CBs and conduction bands (VBs) between TiO₂ and Bi₂O₃ results in a charge transfer of photogenerated electrons and holes, as shown in Fig. 5c. Specifically, the photo-generated holes on the VB of Bi₂O₃ will be transported to that of TiO₂; meanwhile, the photo-generated electrons in the CB of TiO₂ will transfer to that of Bi₂O₃, which can be described to the p-n junction. In this case, the spatially separated holes on Bi₂O₃ and electrons on TiO₂ would possess sufficient energy to thermodynamically induce redox reactions, leading to a charge separation promotion [58,59]. The Z-scheme system of Bi₂O₃/TiO₂, by introduction of the carbon layer, as shown in Fig. 5d, is thus much more favorable for the charge separation by promoting the charge transfer from Bi₂O₃ to TiO₂, consequently further enhancing the photoelectrochemical detection for organics [60].

As a typical double-transfer mechanism process, electrons can accumulate in the CB of Bi₂O₃, which is different with the Z-scheme

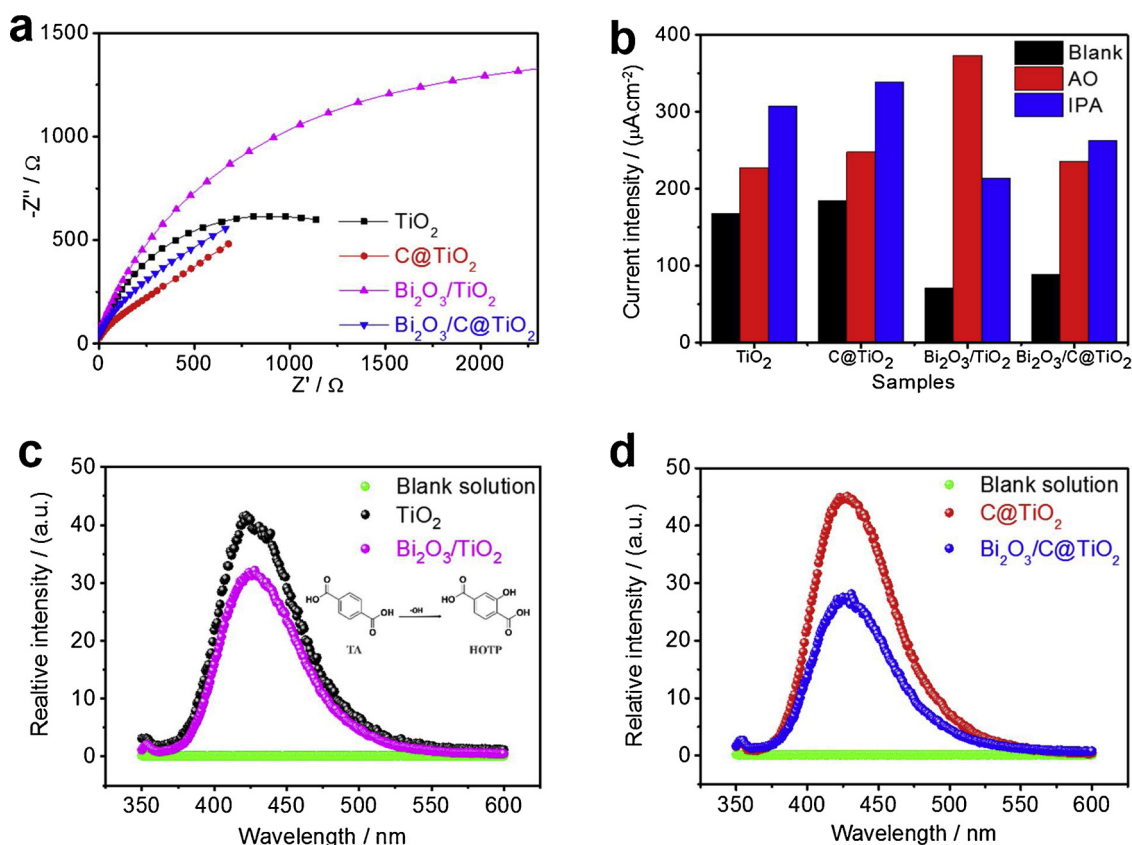


Fig. 4. EIS curves under illumination at 0.1 V (a), trapping experiments for TiO_2 , C@TiO_2 , $\text{Bi}_2\text{O}_3/\text{TiO}_2$ and $\text{Bi}_2\text{O}_3/\text{C@TiO}_2$ NTAs under illumination, respectively; Photoluminescence spectra of terephthalic acid after being illuminated with UV light for TiO_2 , $\text{Bi}_2\text{O}_3/\text{TiO}_2$ (c) and C@TiO_2 , $\text{Bi}_2\text{O}_3/\text{C@TiO}_2$ NTAs (d).

system (Fig. 5d). Hence, we believe that the productivity of $\cdot\text{O}_2^-$ active radicals between $\text{Bi}_2\text{O}_3/\text{TiO}_2$ and $\text{Bi}_2\text{O}_3/\text{C@TiO}_2$ will tell if a novel Z-scheme system is constructed or not. Here, the productivity of $\cdot\text{O}_2^-$ active radicals was investigated by the ESR spectra of $\cdot\text{O}_2^-$ trapped by DMPO, as shown in Fig. 6 [54,57]. The $\text{Bi}_2\text{O}_3/\text{C@TiO}_2$ would not possess a better productivity of $\cdot\text{O}_2^-$ than that of $\text{Bi}_2\text{O}_3/\text{TiO}_2$, if the Z-scheme system was not formed. However, the present results show that the productivity of $\text{Bi}_2\text{O}_3/\text{C@TiO}_2$ for $\cdot\text{O}_2^-$ is higher than that of

$\text{Bi}_2\text{O}_3/\text{TiO}_2$. Therefore, the outstanding performance of $\text{Bi}_2\text{O}_3/\text{C@TiO}_2$ can be attributed to the construction of the Z-scheme system [61–64].

Herein, it can be explained why the modified TiO_2 or C@TiO_2 possesses a lower background photocurrent and higher current response to organics. Firstly, it is known that the background photocurrent of TiO_2 is dependent on the transformation of electrons along the nanotubes to the substrate. Hence, the increase in background photocurrents of C@TiO_2 is ascribed to the enhanced optical absorption

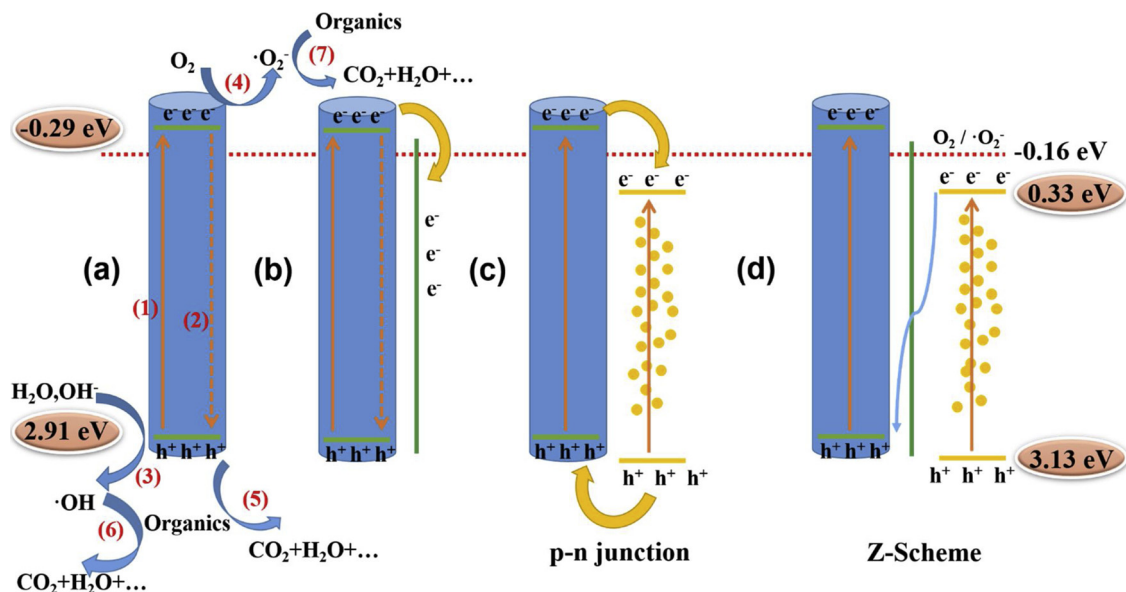


Fig. 5. Proposed mechanism diagram of TiO_2 (a), C@TiO_2 (b), $\text{Bi}_2\text{O}_3/\text{TiO}_2$ (c) and $\text{Bi}_2\text{O}_3/\text{C@TiO}_2$ (d) NTAs.

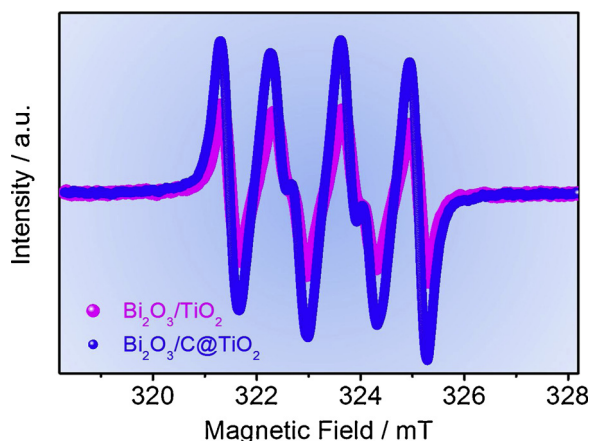


Fig. 6. ESR spectra of $\cdot\text{O}_2^-$ radical trapped by DMPO for $\text{Bi}_2\text{O}_3/\text{TiO}_2$ and $\text{Bi}_2\text{O}_3/\text{C}@\text{TiO}_2$ NTAs respectively.

and low recombination rate of electron-hole pairs. In addition, electrons are more likely to transfer to Ti substrate with the presence of the carbon layer. Lower background photocurrents are obtained with the modification of Bi_2O_3 nanocrystals, which is ascribed to the regulated electrons transfer through the p-n junction and Z-scheme formed. Secondly, the high current response of TiO_2 or $\text{C}@\text{TiO}_2$ NTAs to organics with Bi_2O_3 modification is related to the high separation efficiency and high organic oxidation by holes, instead of the indirect oxidation by forming $\cdot\text{OH}$ radical. The high current responses are different for $\text{Bi}_2\text{O}_3/\text{TiO}_2$ (p-n junction) and $\text{Bi}_2\text{O}_3/\text{C}@\text{TiO}_2$ NTAs (Z-scheme). For $\text{Bi}_2\text{O}_3/\text{TiO}_2$ NTAs system, electrons transfer from TiO_2 to Bi_2O_3 by Bi_2O_3 modification and react with $\cdot\text{OH}$ radicals by “external recombination” method, as reported by a previous study [19]. On the other hand, in the system of $\text{Bi}_2\text{O}_3/\text{C}@\text{TiO}_2$ NTAs, the regulated holes transfer through formed Z-scheme resulting giving rise to the low $\cdot\text{OH}$ productivity of holes, and therefore the high current response can be ascribed to the high reaction ability of direct oxidation by holes on VB of Bi_2O_3 , which is also agreeable with the results of PL. The holes, instead of $\cdot\text{OH}$ radicals, therefore play a more crucial role in the photoelectrochemical determination.

4. Conclusion

A novel carbon-bridged protocol is demonstrated for promoting electron trapping in the p-n $\text{Bi}_2\text{O}_3\text{-TiO}_2$ heterojunction. The carbon-bridged $\text{Bi}_2\text{O}_3@\text{TiO}_2$ nanotube arrays ($\text{Bi}_2\text{O}_3/\text{C}@\text{TiO}_2$ NTAs) are endowed with a highly selective photoelectrochemical determination performance with negligible background photocurrent and strong current detection. As a result, it shows much better determination performance, including the current noise, sensitivity, and detection limit. The results of ESR spectra of $\cdot\text{O}_2^-$ trapped by DMPO help confirm the construction of carbon-bridged Z-scheme. The Z-scheme heterostructured system shows a high charge-separation efficiency, strong redox ability, and the low $\cdot\text{OH}$ productivity of holes due to the carbon bridge effect. The present work represents an alternative model in developing the carbon-bridged Z-scheme heterostructures for highly sensitive and low-cost photoelectrochemical detection. The metal oxides with uniform sizes in the nanometer range and carbon-bridging can be extended to other heterostructure systems.

Acknowledgements

This work was financially supported by the 111 Project “New Materials and Technology for Clean Energy” (B18018) and the Key Technologies R & D Program of Anhui Province (1704c0402195). John Wang acknowledges the support of the National Research Foundation

(NRF, Singapore, 2016NRF-CRP001-023). Mr. Yajun Pang also would like to acknowledge the financial support received from the China Scholarship Council (CSC, 201806690009). Additionally, we thank Instruments’ Center for Physical Science of Hefei National Laboratory for Physical Sciences at the Microscale for the room-temperature ESR measurements.

Appendix A. Supplementary data

Supplementary material related to this article can be found, in the online version, at doi:<https://doi.org/10.1016/j.apcatb.2019.01.077>.

References

- [1] A. Fujishima, K. Honda, *Nature* 238 (1972) 37–38.
- [2] J. Liu, D. Jared, *Nature* 435 (2005) 1179–1186.
- [3] Y. Kim, S. Sasaki, K. Yano, K. Ikebukuro, K. Hashimoto, I. Karube, *Anal. Chim. Acta* 432 (2001) 59–66.
- [4] D.M. Dharmadhikari, A.P. Vanerker, N.M. Barhate, *Environ. Sci. Technol.* 39 (2005) 6198–6201.
- [5] Q. Zheng, B. Zhou, J. Bai, L. Lin, Z. Jin, J. Zhang, J. Li, Y. Liu, W. Cai, X. Zhu, *Adv. Mater.* 20 (2008) 1044–1049.
- [6] Z. Wu, Y. Wang, L. Sun, Y. Mao, M. Wang, C. Lin, *J. Mater. Chem. A* 2 (2014) 8223–8229.
- [7] J.M. Macak, B.G. Gong, M. Hueppe, P. Schmuki, *Adv. Mater.* 19 (2007) 3027–3031.
- [8] I. Paramasivam, H. Jha, N. Liu, P. Schmuki, *Small* 8 (2012) 3073–3103.
- [9] L.X. Zheng, S.C. Han, H. Liu, P.P. Yu, X.S. Fang, *Small* 12 (2016) 1527–1536.
- [10] H. Zhang, R. Zong, J. Zhao, Y. Zhu, *Environ. Sci. Technol.* 42 (2008) 3803–3807.
- [11] T. Sharifi, Y. Ghayeb, T. Mohammadi, M.M. Momeni, *Dalton Trans.* 47 (2018) 11593–11604.
- [12] C.X. Feng, G.Q. Xu, H.P. Liu, J. Lv, Z.X. Zheng, Y.C. Wu, *J. Electrochem. Soc.* 161 (2014) H57–H61.
- [13] P. Roy, S. Berger, P. Schmuki, *Angew. Chem. Int. Ed.* 50 (2011) 2904–2939.
- [14] J. Su, L. Zhu, G. Chen, *Appl. Catal. B Environ.* 186 (2016) 127–135.
- [15] W.J. Zhong, S.B. Sang, Y.Y. Liu, Q.M. Wu, K.Y. Liu, H.T. Liu, *J. Power Sources* 294 (2015) 216–222.
- [16] K. Zhu, N.R. Neale, A. Miedaner, A.J. Frank, *Nano Lett.* 7 (2007) 69–74.
- [17] H. Li, Z.B. Xia, J.Q. Chen, L. Lei, J.H. Xing, *Appl. Catal. B: Environ.* 168 (2015) 105–113.
- [18] M.M. Momeni, Y. Ghayeb, N. Moosavi, *Nanotechnology* 29 (2018) 425701.
- [19] Y.J. Pang, G.Q. Xu, C.K. Fang, J. Lv, J.Q. Liu, Y.C. Wu, *RSC Adv.* 6 (2016) 61367–61377.
- [20] N.L. Reddy, S. Min, M. Valant, M.V. Shankar, *Int. J. Hydrog. Energy* 42 (2017) 6627–6636.
- [21] J. Hou, C. Yang, Z. Wang, S. Jiao, H. Zhu, *Appl. Catal. B Environ.* 129 (2013) 333–341.
- [22] Y. Cui, H. Zhang, R. Guo, Q. Ma, X. Deng, X. Deng, X. Cheng, X. Li, M. Xie, Q. Cheng, C. Zou, *Electrochim. Acta* 246 (2017) 1075–1081.
- [23] D. Li, Y. Zhang, Y. Zhang, X. Zhou, S. Guo, J. Hazard. Mater. 258–259 (2013) 42–49.
- [24] R. He, D. Xu, B. Cheng, J. Yu, W. Ho, *Nanoscale Horiz.* 3 (2018) 464–504.
- [25] H.M. Zhu, B.F. Yang, J. Xu, Z.P. Fu, M.W. Wen, T. Guo, S.Q. Fu, J. Zuo, S.Y. Zhang, *Appl. Catal. B Environ.* 90 (2009) 463–469.
- [26] H.J. Li, Y.Y. Gao, Y. Zhou, F.T. Fan, Q.T. Han, Q.F. Xu, X.Y. Wang, M. Xiao, C. Li, Z.G. Zou, *Nano Lett.* 16 (2016) 5547–5552.
- [27] K. Xie, Q. Wu, Y. Wang, W. Guo, M. Wang, L. Sun, C. Lin, *Electrochim. Commun.* 13 (2011) 1469–1472.
- [28] N.K. Veldurthi, N.K. Eswar, S.A. Singh, G. Madras, *Appl. Catal. B Environ.* 220 (2018) 512–523.
- [29] J.J. Xian, D.Z. Li, J. Chen, X.F. Li, M. He, Y. Shao, L.H. Yu, J.L. Fang, *ACS Appl. Mater. Int.* 6 (2014) 13157–13166.
- [30] K. Iwashina, A. Iwase, Y.H. Ng, R. Amal, A. Kudo, *J. Am. Chem. Soc.* 137 (2015) 604–607.
- [31] L.X. Yang, Z.Y. Li, H.M. Jiang, W.J. Jiang, R.K. Su, S.L. Luo, Y. Luo, *Appl. Catal. B Environ.* 183 (2016) 75–85.
- [32] F.J. Wu, X. Li, W. Liu, S.T. Zhang, *Appl. Surf. Sci.* 405 (2017) 60–70.
- [33] X.K. Zeng, Z.Y. Wang, G. Wang, T.R. Gengenbach, D.T. McCarthy, A. Deletic, J.G. Yu, X.W. Zhang, *Appl. Catal. B Environ.* 218 (2017) 163–173.
- [34] H.P. Liu, G.Q. Xu, J.W. Wang, J. Lv, Z.X. Zheng, Y.C. Wu, *Electrochim. Acta* 130 (2014) 213–221.
- [35] J.G. Kim, S.H. Lee, S.H. Nam, S.M. Choi, W.B. Kim, *RSC Adv.* 2 (2012) 7829–7836.
- [36] C.P. Yu, Y. Wang, J.F. Zhang, X. Shu, J.W. Cui, Y.Q. Qin, H.M. Zheng, J.Q. Liu, Y. Zhang, Y.C. Wu, *New J. Chem.* 40 (2016) 6881–6889.
- [37] J.J. Hu, G.Q. Xu, J.W. Wang, J. Lv, X.Y. Zhang, T. Xie, Z.X. Zheng, Y.C. Wu, *Dalton Trans.* 44 (2015) 5386–5395.
- [38] V.V. Belousov, I.V. Kulbakin, S.V. Fedorov, A.A. Klimashin, *ACS Appl. Mater. Int.* 8 (2016) 22324–22329.
- [39] J.S. Lee, K.H. You, C.B. Park, *Adv. Mater.* 24 (2012) 1084–1088.
- [40] D. Li, J.L. Jia, T. Zheng, X.W. Cheng, X.J. Yu, *Appl. Catal. B Environ.* 188 (2016) 259–271.
- [41] Y. Fang, Y.Y. Lv, R.C. Che, H.Y. Wu, X.H. Zhang, D. Gu, G.F. Zheng, D.Y. Zhao, *J. Am. Chem. Soc.* 135 (2013) 1524–1530.

- [42] P. Song, X.Y. Zhang, M.X. Sun, X.L. Cui, Y.H. Lin, *Nanoscale* 4 (2012) 1800–1804.
- [43] M.Z. Ge, C.Y. Cao, S.H. Li, S.N. Zhang, S. Deng, J.Y. Huang, Q.S. Li, K.Q. Zhang, S.S. Al-Deyab, Y.K. Lai, *Nanoscale* 7 (2015) 11552–11560.
- [44] J. Zhu, S.H. Wang, J.G. Wang, D.Q. Zhang, H.X. Li, *Appl. Catal. B Environ.* 102 (2011) 120–125.
- [45] D.H. Wang, L. Jia, X.L. Wu, L.Q. Lu, A.W. Xu, *Nanoscale* 4 (2012) 576–584.
- [46] Q. Hao, R.T. Wang, H.J. Lu, C. Xie, W.H. Ao, D.M. Chen, C. Ma, W.Q. Yao, Y.F. Zhu, *Appl. Catal. B Environ.* 219 (2017) 63–72.
- [47] J. Zhong, C. Feng, J.L. Zhang, *J. Phys. Chem. C* 114 (2009) 933–939.
- [48] W.J. Ren, Z.H. Ai, F.L. Jia, L.Z. Zhang, X.X. Fan, Z.G. Zou, *Appl. Catal. B Environ.* 69 (2007) 138–144.
- [49] J. Wu, Y. Sun, C. Gu, T. Wang, Y. Xin, C. Chai, C. Cui, D. Ma, *Appl. Catal. B Environ.* 237 (2018) 622–632.
- [50] X.Y. Zhang, D.Li.L. Bourgeois, H.T. Wang, P.A. Webley, *ChemPhysChem* 10 (2009) 436–441.
- [51] J. Luo, Q. Ma, H. Gu, Y. Zheng, X. Liu, *Electrochim. Acta* 173 (2015) 184–192.
- [52] M.Y. Wang, D.J. Zheng, M.D. Ye, C.C. Zhang, B.B. Xu, C.J. Lin, L. Sun, Z.Q. Lin, *Small* 11 (2015) 1436–1442.
- [53] H.L. Lin, J. Cao, B.D. Luo, B.Y. Xu, S.F. Chen, *Catal. Commun.* 21 (2012) 91–95.
- [54] Y.C. Deng, L. Tang, G.M. Zeng, C.Y. Feng, H.R. Dong, J.J. Wang, H.P. Feng, Y.N. Zhou, Y. Pang, *Environ. Sci. Nano* 4 (2017) 1494–1511.
- [55] S. Eremia, D. Chevalier-Lucia, G. Radu, J. Marty, *Talanta* 77 (2008) 858–862.
- [56] Y. Gong, D.P. Wang, R. Wu, S. Gazi, H.S. Soo, T. Sriharan, Z. Chen, *Dalton Trans.* 46 (2017) 4994–5002.
- [57] Y. Nosaka, A.Y. Nosaka, *Chem. Rev.* 117 (2017) 11302–11336.
- [58] J.L. Hu, C.J. Huang, M. Liu, X.Q. Qiu, *Appl. Catal. B Environ.* 142 (2013) 598–603.
- [59] Y.Q. Cui, H.X. Zhang, R.N. Guo, Q.L. Ma, X.Y. Deng, X.W. Cheng, X.L. Li, M.Z. Xie, Q.F. Cheng, C.W. Zou, *Electrochim. Acta* 246 (2017) 1075–1081.
- [60] J.S. Wang, C.L. Qin, H.J. Wang, M.N. Chu, A. Zada, X.L. Zhang, J.D. Li, F. Raziq, Y. Qu, L.Q. Jing, *Appl. Catal. B Environ.* 221 (2018) 459–466.
- [61] D. Ma, J. Wu, M.C. Gao, Y.J. Xin, Y.Y. Sun, T.J. Ma, *Chem. Eng. J.* 313 (2017) 1567–1576.
- [62] P. Zhou, J.G. Yu, M. Jaroniec, *Adv. Mater.* 26 (2014) 4920–4935.
- [63] G. Yang, D. Chen, H. Ding, J. Feng, J.Z. Zhang, Y. Zhu, S. Hamid, D.W. Bahnemann, *Appl. Catal. B Environ.* 219 (2017) 611–618.
- [64] G. Zhou, M.F. Wu, Q.J. Xing, F. Li, H. Liu, X.B. Luo, J.P. Zou, J.M. Luo, A.Q. Zhang, *Appl. Catal. B Environ.* 220 (2018) 607–614.